

STag: A Stable Fiducial Marker System

Burak Benligiray Cihan Topal Cuneyt Akinlar

Abstract

In this paper, we propose STag, a fiducial marker system that provides stable pose estimation. The outer square border of the marker is used for detection and pose estimation. This is followed by a novel pose refinement step using the inner circular border. The refined pose is more stable and robust across viewing conditions compared to the state of the art. In addition, the lexicographic generation algorithm is adapted for fiducial markers, and libraries with various sizes are created. This makes the system suitable for applications that require many unique markers, or few unique markers with high occlusion resistance. The edge segment-based detection algorithm is of low complexity, and returns few false candidates. These features are demonstrated with experiments on real images, including comparisons with the state of the art fiducial marker systems.

1 Introduction

The image projection of an object depends on its pose. If different projections of the object create distinguishable appearances, its pose can be estimated using vision. Highly symmetrical objects look similar with different poses, which causes ambiguity, and less symmetrical objects need to be represented by complex models, which increases the computational cost [1, 2]. Where processing cost and accuracy are the most critical factors, the best solution is to use a reference object whose pose can be easily and unambiguously estimated with vision.

Fiducial markers are printable patterns that combine fast and accurate pose estimation with easy and inexpensive deployment [3], which is particularly useful for prototyping. They were first proposed to be used for augmented reality [4, 5, 6], and are still relevant in the recent virtual reality boom [7]. In addition, they see increasing use in systems that require to interact precisely and responsively with the real world, including robotics [8, 9, 10].

Precision is a pose estimation quality metric that is often overlooked in favor of accuracy. However, in some applications, the stability provided by precision is critical. For example, when using the estimated pose to render graphics for a mixed reality application, the jitter caused by the instability will be more immersion breaking than a constant misalignment. Similarly, if we are using

Source code: <https://github.com/bbenligiray/stag>

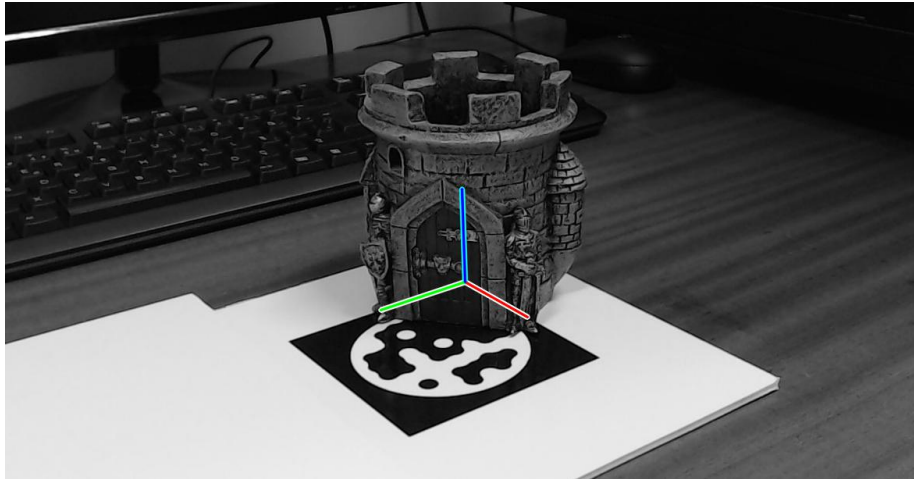


Figure 1: An occluded marker is detected and its relative coordinate axes are drawn using the estimated pose.

the estimated pose for control, the instability may cause oscillatory behavior. Therefore, fiducial marker systems should aim to improve stability along with the usual performance factors, such as detection robustness, speed and library size.

In this paper, we propose STag, a fiducial marker system that provides stable localization without using any temporal filtering. This is achieved by the hybrid marker design seen in Figure 1. The outer square border is used for detection and pose estimation, and the inner circular border is used to refine the estimated pose. Since both of these features are simple, they do not degrade when seen from long distances and acute viewing angles, resulting in robust detection. The pose refinement step that provides stability is unique in that it uses a single conic correspondence to estimate the homography, with the help of a very good starting point for the optimization. To support the use of a wide range of numbers of markers, we generated various marker libraries by adapting the lexicographic generation algorithm. The edge segment-based marker detection algorithm runs in real-time and returns few false positives.

2 Related Work

Matrix [4] is the first example of the square barcode type fiducial marker. Its square border and 2D matrix encoding seen in Figure 2a has since become the default fiducial marker design. Marker detection algorithms return many candidates that agree with the general shape of the marker. Matrix uses cyclic redundancy check to validate these candidates.

ARToolkit [11] markers are encoded with patterns chosen by the user, each of which is associated with an ID (see Figure 2b). These patterns are densely

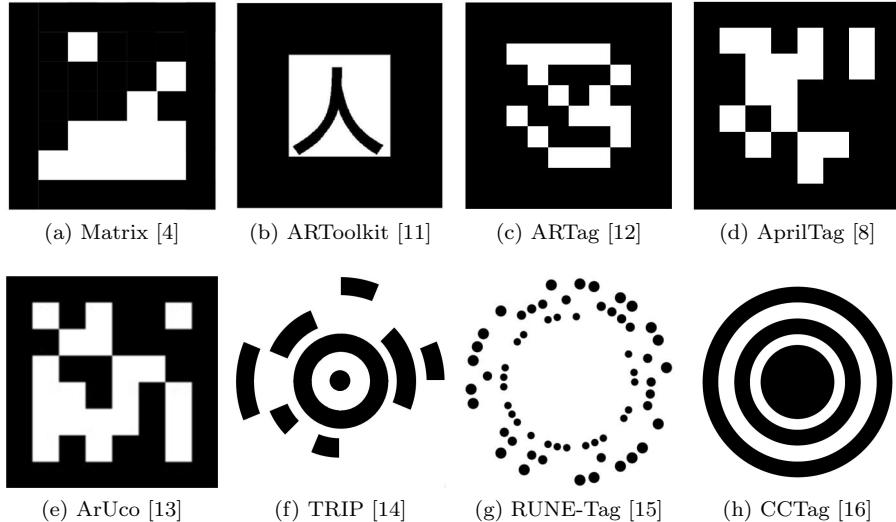


Figure 2: Marker designs of some notable fiducial marker systems in the literature.

sampled and decoded using a nearest neighbor method. This approach has error detection and correction functionality, but its performance depends on the specific set of patterns in the library. Matrix-like coding option is added to ARToolkit with an extension [17].

ARTag [12] is the first marker system with forward error correction capability based on digital coding methods (see Figure 2c). This influenced the following studies to place a heavier emphasis on coding. Additionally, ARTag is the first marker system to detect markers from edges.

AprilTag [8] shares the square barcode type design (see Figure 2d), but the user chooses the size of the encoding grid. Other recent marker systems also provide marker variants with different bandwidths [18, 13]. AprilTag is the first marker system to use lexicodes, greedily generated codes with error detection and correction capabilities.

ArUco [13] has the unique feature of calculating an occlusion mask with tiled markers, which can prove useful in mixed reality applications (see Figure 2e). The original ArUco marker library is created using a stochastic lexicode generation algorithm. Better libraries are added using a mixed integer linear programming approach [19].

TRIP [14] uses a circular design (see Figure 2f). Markers have a ring in the middle for detection, and two outer rings for binary encoding. Outer rings are divided into aligned slices. The black slice pair indicates the starting point of the encoding. Relying on singular features to resolve rotation ambiguity for circular designs is not unique to TRIP [20, 21]. Having such regions is not preferable, as occluding them will prevent the marker from being detected.

RUNE-Tag [15, 18] does not have a border in the traditional sense. The coding dots are arranged in a circular shape, and act as candidate generating features (see Figure 2g). The pose is estimated by using the coding dots as point correspondences. This approach results in a finite pose ambiguity similar to square markers, which can be resolved by decoding. Due to the large number of coding dots used as correspondences, RUNE-Tag provides high pose estimation accuracy. There is also a square shaped variant of the same concept [22].

CCTag [16] is an improvement over the concentric circles commonly used for camera calibration (see Figure 2h). Its main contribution is robustness against motion blur, an important issue in tracking applications. CCTag does not estimate the pose of the marker, but only locates the projection of the marker center, similar to some earlier circular fiducial markers [23].

3 Marker Design

The proposed marker design consists of two parts, the border and the encoding area. Similar to many marker systems, an outer square border is used for candidate detection and pose estimation. Additionally, an inner circular border is introduced for pose refinement. The encoding area is densely packed with circular bit representations.

3.1 Border

Square borders are very popular in fiducial marker design, because they allow for simple solutions. In nearly all square bordered markers, code bits are represented by squares tiled in a grid pattern. The four corners of the border provide enough correspondences for an exact solution of the marker’s homography [24]. The correspondence is finitely ambiguous, but this ambiguity is resolved by decoding.

Marker systems that use circular borders have failed to converge to a widely accepted set of solutions. Code bits are represented by irregular shapes, rather than equally sized squares or disks [14, 20]. Moreover, there is no universal tiling scheme similar to the grid pattern. Circular borders are also problematic for pose estimation. A single circle–ellipse correspondence is not sufficient to estimate the marker’s homography [25]. An additional point correspondence can be used to resolve the ambiguity [14, 21]. A singular rotation indicating feature is a critical point of failure, thus is not desirable. Despite these problems, there is an advantage of using a circular border: The projection of a circle can be localized more accurately than the projection of a square [26].

We propose these border types to be used in combination (see Figure 3a). The outer square border is used to localize the marker and estimate its pose. After validating the marker by decoding, the estimated pose is refined using the inner circular border.

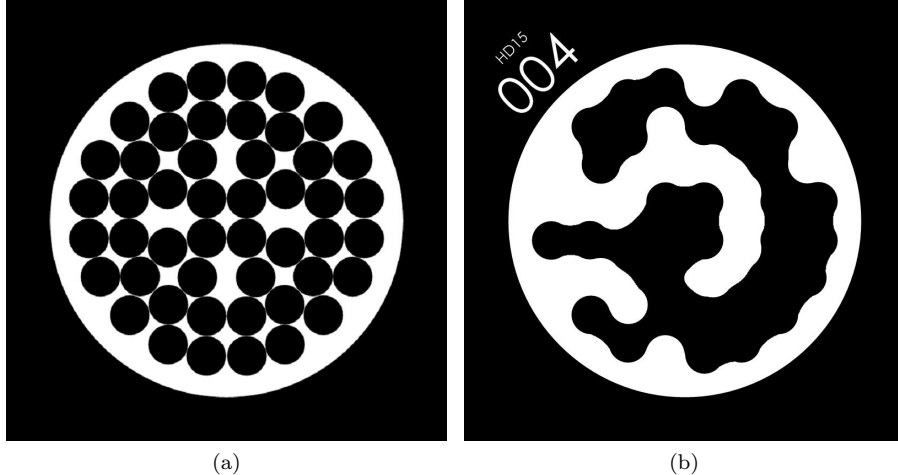


Figure 3: (a) Four-fold symmetric tiling with 48 disks. (b) Marker number 4 from 15 minimum Hamming distance library.

3.2 Encoding Area

Marker systems in the literature focus on digital coding methods, yet their graphical implementation is often overlooked. In this section, we will discuss bit representations and their tiling.

Ideally, the detection algorithm samples the center of the bit representations. However, the error in candidate localization causes the samplings to be off center. A disk accommodates for errors in all directions equally. It is more appropriate to represent bits as disks, rather than squares. SCR is an example of a marker design where this approach is used [6]. A dense packing of disks in the circular encoding area is the ideal tiling scheme for our design.

There is a subtle constraint on the packing scheme. It must be four-fold rotationally symmetric, such that it aligns with its rotations of multiples of 90° . This way, we can determine what a marker code reads from the three incorrect rotations. Then, the coding scheme can be designed to specifically invalidate these incorrect readings. To satisfy this symmetry, we pack disks in a quadrant of a circle, and replicate this packing rotationally.

It is predictable that the densest packing of disks in a quadrant of a circle will be irregular, i.e., not in a lattice-like pattern. We searched for this irregular packing using a simulated annealing algorithm [27]. A fixed number of small disks are manually placed in a quadrant to speed up the process. Then, these disks are iteratively perturbed and enlarged with decreasing intensity. We experimented with different number of disks, and found that 48 disks can be packed particularly densely. 48-bit long codewords are also suitable for the lexicode generation method described in Section 4. The resulting tiling scheme is seen in Fig. 3a.



Figure 4: A marker with ambiguous rotation has four circularly permuted readings.

In most marker designs, there are no gaps between neighboring bits. While its positive effect is difficult to quantify, it improves robustness against blooming and reflection effects, especially when the printing material is glossy. To fill the gaps, the code pattern is morphologically dilated and eroded repeatedly. A resulting example marker is presented in Fig. 3b.

4 Coding

The detector reads the marker code by sampling the captured image. This process can be seen as one-way communication over a noisy channel. Some bits of the code may be flipped, either due to incorrect thresholding or occlusion. The most critical role of the coding scheme is to do error detection, which eliminates non-markers and markers with unreadable codes. Additionally, corrupted codes should be corrected where possible.

The coding scheme has to solve a marker-specific problem, which is the rotation ambiguity. By only using the square border of a marker, we estimate four possible poses. A different codeword is read for each pose (see Figure 4). If decoding is to resolve the rotation ambiguity, only one of these codewords must be valid.

The lexicode generation algorithm tests potential codewords and chooses the ones that satisfy an arbitrary constraint. For the traditional version, this constraint is that if a codeword is to be selected, it should be at least a predetermined Hamming distance away from the previously chosen codewords [28]. This can be adapted to marker lexicode generation by also testing for the circular permutations of the codewords.

The described lexicode generation algorithm is an exhaustive search of an n -dimensional binary space, n being the length of the codewords. This corresponds to a time complexity of $O(2^n)$. With 48-bit long codewords, the algorithm requires an unreasonable amount of time to finish, even with a GPU implementation. To overcome this problem, we took a hierarchical approach.

Table 1: STag library sizes with respective minimum Hamming distances.

Min. HD	11	13	15	17	19	21	23
Library Size	22309	2884	766	157	38	12	6

Note that in Figure 4, the codeword is composed of four sub-codewords. We generated sub-codewords of 12 bits, then concatenated them to build the final codewords.

Generating n -bit long lexicodes with d minimum Hamming distance is similar to packing hyperspheres of radius d in an n -dimensional space [29]. It is shown that with certain n and d , an irregular packing may be denser than the optimal regular packing [30]. Since greedy algorithms such as lexicode generation follow a regular pattern, we should avoid such parameters. In our case, the number of bits in a sub-codeword, n , is 12. By experimentation, we have seen that a d of 4 has resulted in a very dense packing with 128 different sub-codewords.

Each of the sub-codewords can be regarded as a digit in base-128. Different base-128 digits have at least 4 Hamming distance, but the exact distance depends on which two digits are considered. Using the base-128 digits, we generated 4-digit long lexicodes with d minimum Hamming distance. Differently from the first step, we had to check the circular permutations, as base-128 digits overlap with each other with different rotations (as in Figure 4).

After generating 4-digit long lexicodes, base-128 digits are replaced with the corresponding sub-codewords to obtain 48-bit long codewords. Codewords less than d Hamming distance away from all ones or all zeros are eliminated. The bits of all codewords are shuffled with the same permutation to scramble unintentional patterns.

With a minimum Hamming distance of $2e + 1$, e bit error correction can be implemented. Even when the error correction will not be used, the increased distance reduces intermarker confusion rate. On the other hand, larger marker libraries have smaller minimum Hamming distances. Therefore, it is preferable to use the smallest marker library possible to benefit from the largest minimum Hamming distance. We generated libraries with different sizes and Hamming distances to accommodate for a variety of applications. Smaller libraries with higher minimum Hamming distances can be used for small-scale AR applications where occlusion is common. Larger libraries are more suitable for navigation through large interior spaces or inventory applications. The resulting library sizes are presented in Table 1.

4.1 Library Comparison

The number of unique markers needed for an application is usually inflexible. The main performance metric for a coding scheme is the amount of error correction it can provide for various library sizes. Bit error ratio (BER) is the number of error bits divided by the number of total bits. A marker library that

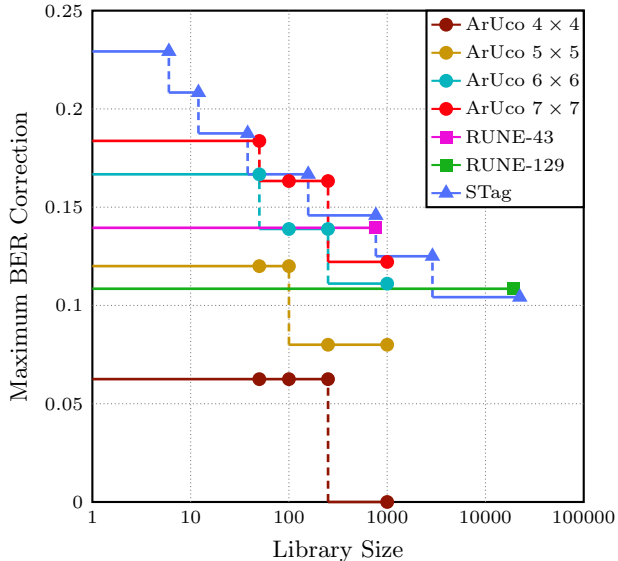


Figure 5: Marker libraries with different sizes and maximum bit error ratio (BER) correction capabilities.

can correct 0.1 BER will work when at most 10% of the coding area is read incorrectly. By using this metric, we can compare libraries with different code lengths.

See Figure 5 for a comparison of ArUco [19], RUNE-Tag [15] and STag libraries. Marker variants with different code lengths are plotted separately. The horizontal axis is in logarithmic scale, because improving error correction capability reduces library size exponentially.

ArUco variants grow more efficient with longer codewords. Both RUNE-Tag libraries are efficient, but they do not provide the best performance across the whole scale. ArUco 7×7 , RUNE-129 and STag libraries lie on the same line, which implies a theoretical upper bound. STag libraries cover a large range of library sizes, and provide the best or near-best performance.

5 Detection Algorithm

The algorithm starts by detecting quadrilaterals as candidates. The homography of each candidate is estimated to read its code. The codes are used to eliminate non-marker candidates and determine the rotation of true candidates. The poses of the validated candidates are refined using the inner circular borders.

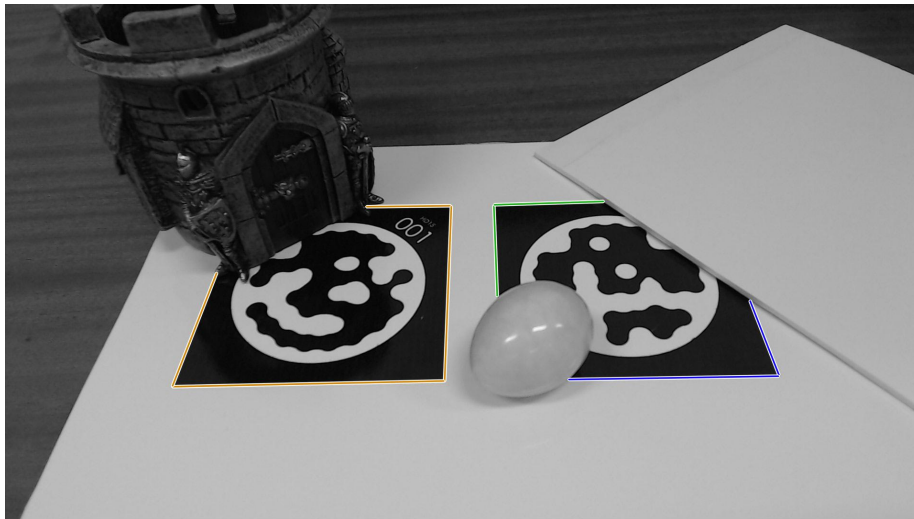


Figure 6: Line segments detected on the same edge segment are drawn with the same color. Only the marker on the left can be detected, because its vertices lie on a single edge segment.

5.1 Candidate Detection

Matrix’s detection algorithm starts by binary thresholding, on the basis that it performs well with high contrast markers [4]. Fiala argues that binary thresholding is susceptible to bad lighting and occlusion, thus is not suitable for marker detection [31]. Edge detection was proposed as a more reliable alternative [12, 8], but even the most recent marker systems still opt for thresholding [13]. We agree with both sides in this issue, edges are suitable features for candidate detection, but the high contrast marker design should be exploited.

Assuming a pinhole camera model, a square appears as a simple convex quadrilateral (quad) in the image [24]. A quad can be defined using four line segments. Where n line segments are detected, four combinations of these line segments will result in $O(n^4)$ possible quads. As the number of detected line segments increase due to resolution and scene complexity, it becomes infeasible to validate all such candidates.

EDPF extracts pixel-wide contiguous edge segments by tracing through sparse edge pixels, and validates them based on the Helmholtz principle [32]. The resulting edge segments along the marker borders tend to be continuous due to the contrast. We use EDLines [33] to detect line segments on the edge segments. By limiting the quad search to consecutive line segments detected on individual edge segments, candidate detection complexity drops to $O(n)$.

The proposed method still works when the edge segment surrounding the marker is broken. In Figure 6, we see two partially occluded markers. The one on the left is occluded at a single point. The visible part of the border is

still detected as a single edge segment, thus the resulting line segments can be combined to form a quad. The marker on the right is occluded at two points. In this case, the line segments extracted from the border lie on different edge segments, and cannot be combined. Therefore, the proposed candidate detection algorithm is not resistant against separate occlusions at two or more vertices.

5.2 Homography Estimation and Decoding

We estimate the homography matrix, H , of a candidate by using its corners as correspondence points for direct linear transform [24]. There are four ways of matching the corresponding corners, of which an arbitrary one is used. The projections of bit representations are sampled using this homography to obtain the embedded codeword.

We keep all codewords in the library and their circular rotations in a list. The read codeword is compared with each element in the list by XORing and doing a population count. If the Hamming distance between the read codeword and a codeword in the list is smaller than or equal to the maximum number of bits to be corrected, the respective rotation and ID is associated with the candidate. If the arbitrarily chosen rotation is found to be incorrect, the homography is updated with the correct correspondence.

5.3 Pose Refinement

At this point, we have a set of markers that are validated by decoding. We will localize the inner circular borders, and use them to refine the estimated poses.

5.3.1 Ellipse Localization

Our objective is to identify the edge segment loop extracted from the inner circular border, and fit an ellipse to it. We assume that marker corners are localized with some error. In Figure 7a, we presented an example with exaggerated localization error for better viewing. Due to the corner localization error, both the estimated homography and the expected ellipse location will be slightly incorrect.

We first find the edge segment loops inside the marker detection (see Figure 7b) and back project them to the marker plane (see Figure 7c). It is expected that among the edge segment loops, the one from the border ellipse will be the most similar to the inner circular border. We estimate this similarity by sparsely sampling the distances between the inner circular border and back projected edge segment loops. An ellipse is fitted to the edge segment loop whose back projection is the most similar to the inner circular border [34] (see Figure 7d).

We detect the absence of a suitable edge segment loop by thresholding the similarity between the back projected edge segment loops and the inner circular border. Since this metric is calculated in the marker plane, the shape and size of the detection is normalized. Thus, the threshold acts equivalently in all poses.

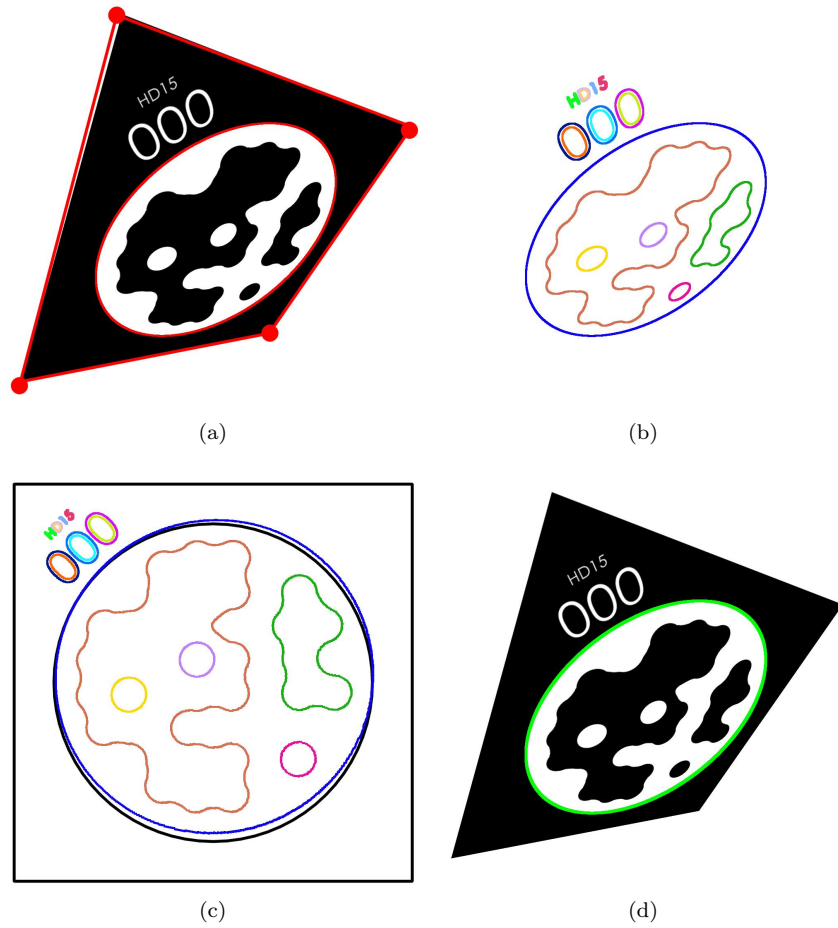


Figure 7: (a) A marker with incorrectly localized corners and the respective expected ellipse location. (b) Edge segment loops inside the marker detection. (c) Edge segment loops back projected to the marker plane. (d) The ellipse fitted to the chosen edge segment loop.

5.3.2 Nonlinear Optimization

Let us call the inner border circle in the marker plane C . We localized the projection of C as an ellipse, which we will call C' (shown in Figure 7d). When we back project C' to the marker plane, we get an ellipse on the marker plane, \tilde{C} , as in Equation 1.

$$\tilde{C} = H^T C' H \quad (1)$$

\tilde{C} does not coincide with C perfectly because of the mislocalization of marker corners (similar to Figure 7c). Our aim is to define a function that quantifies this difference, and refine H by minimizing it. Since the difference metric between the back projected ellipse and the inner circular border has to be repeated at every iteration of the optimization, it should be easily calculable. Where a is the semi-major axis of \tilde{C} , b is the semi-minor axis of \tilde{C} , (e_x, e_y) is the center of \tilde{C} , r is the radius of C and (c_x, c_y) is the center of C , the metric we propose is given in Equation 2. These distances are in the original marker plane, thus they are normalized for pose.

$$\epsilon = \sqrt{(e_x - c_x)^2 + (e_y - c_y)^2 + (a - r)^2 + (b - r)^2} \quad (2)$$

A single circle–ellipse correspondence is not adequate to estimate the homography of a marker. We use the homography estimated using the corners as a starting point, and minimize ϵ in Equation 2 using the Nelder–Mead method [35]. This way, the previously estimated homography is refined such that the ellipse detection is back projected directly on the inner circular border. Since the ellipse is localized more accurately than the marker corners, this improves the stability of the localization.

Let us illustrate the benefit of the pose refinement step with an experiment. A 10 cm-wide marker is positioned 100 cm away from the camera. 1000 consecutive images with a resolution of 1920×1080 are captured from a series of viewing angles. The stability of the detection is represented by the standard deviation of the center localization. See Figure 8 for the results. Before refinement, the marker center is unstable. Moreover, the localization is not robust against the changes in viewing angles. The center of the ellipse we have located in Section 5.3.1 is significantly more stable. After pose refinement, the marker center gains stability across all viewing angles.

6 Comparative Experiments

We compared the proposed marker system with ArUco [13] and RENE-Tag [15] in a series of experiments. These state of the art marker systems are comparable with ours, in that they both provide large libraries and allow pose estimation with a single marker.

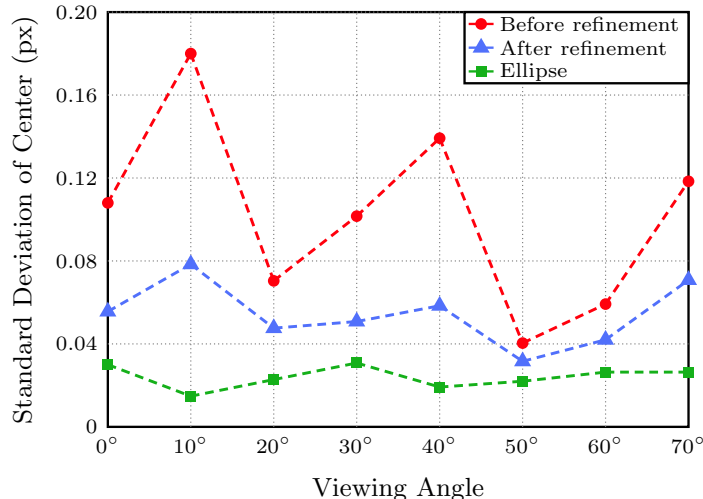


Figure 8: Standard deviation of centers with various viewing angles. The ellipse is more stable than the quad, hence using it to refine the pose stabilizes the marker center.

Table 2: Number of candidates and running time per image in the scene recognition dataset [36].

	ArUco [13]	RUNE-Tag [15]	STag
No. of Candidates	20.3	0	4.0
Time (ms)	20.1	357.8	12.9

6.1 Detection Algorithm in Markerless Case

A detection algorithm should not detect markers in markerless scenes. Fiala uses videos captured in a laboratory and a movie as examples of markerless conditions [12]. Using video sequences inflate the number of test images, because sequential frames are too similar. Instead, we used an indoor scene recognition dataset with 15620 images from 67 categories [36].

6.1.1 Candidate Detection

A marker candidate is a detection whose validity is to be decided by decoding. The code sampled from a non-marker candidate may be validated accidentally, thus each non-marker candidate poses a risk. Detection algorithms that produce lesser number of non-marker candidates will result in lesser number of false positives with the same coding scheme. Moreover, detecting lesser number of candidates will reduce the processing load of the algorithm. See Table 2 for the number of candidates each algorithm detects per frame.

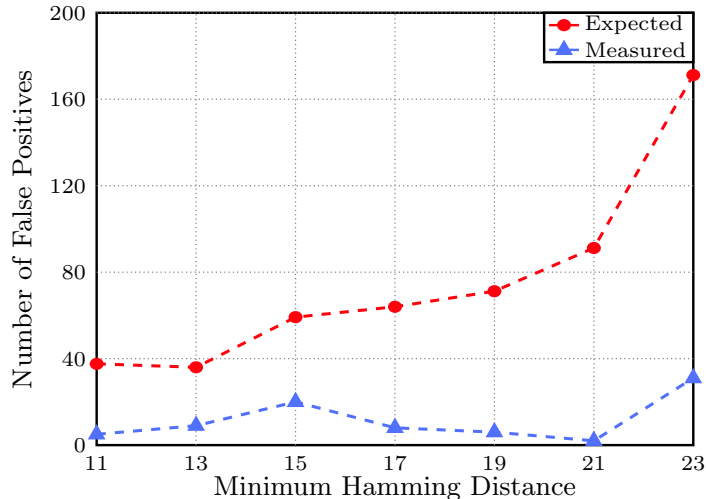


Figure 9: The expected and measured number of false positives in the markerless scene dataset [36] using various STag libraries and respective maximum error correction capabilities.

ArUco detects a very large number of candidates at each frame, which poses a high false positive risk. RUNE-Tag detects an average of 85 ellipses per frame, but candidates produced from the combinations of these ellipses are all eliminated before reaching the decoding stage. False positive resistance in markerless scenes is a valuable feature, but RUNE-Tag is not false positive-proof. When we run the detection algorithm on the image of a RUNE-tag marker, we see that the decoding function is called 149 times. In other words, RUNE-Tag may be susceptible to false positives when there are markers on the scene. STag algorithm detects markers using their square shape, which occurs abundantly in built environments. Nevertheless, we see that the number of candidates that has to be validated is small.

Marker detection algorithms are inherently parallelizable. To nullify the effects of different parallel implementations, we used a single core of a 3.70 GHz Intel Xeon processor to run the algorithms. The dataset images are of 640×480 or lower resolution, but the scenes are cluttered. See Table 2 for average running times per image. We can see that both ArUco and STag perform in real-time, while RUNE-Tag is considerably slower.

6.1.2 Candidate Validation

Detecting a smaller number of non-marker candidates is better. However, we still have to invalidate them by decoding. Fiala assumes that the code sampled from a non-marker candidate is composed of independent random bits [12]. Given that the code length is n , marker library size is N and maximum number

of bits that can be corrected is e , the probability of a non-marker candidate being validated as a false positive is given in Equation 3.

$$P(FP) = 4 \frac{N \sum_{i=0}^e \binom{n}{i}}{2^n} \quad (3)$$

We have already measured the expected number of candidates per frame, $E[Cand]$ (see Table 2). If Fiala’s assumption is correct, we can estimate the expected number of false positives per frame, $E[FP]$, as in Equation 4.

$$E[FP] = E[Cand] P(FP) \quad (4)$$

See Figure 9 for the expected and measured number of false positives in the markerless scene dataset [36] using various STag libraries. The expected number of false positives increases with minimum Hamming distance. Going back to the hypersphere packing analogy for lexicode generation, we can say that hyperspheres are packed more densely when they are larger, such that a random point chosen in binary space is more likely to fall inside one of them. The measured numbers of false positives are quite less than expected, which is desirable. This advantage is likely caused by the elimination of codewords too similar to all ones or all zeros.

Finally, let us discuss the false positive rates of RUNE-Tag and ArUco. Since RUNE-Tag does not detect any candidates, it also does not detect any false positives. Similar to STag, ArUco’s false positive rate depends on the specific marker library used. However, the relationship between false positive rate and library size is highly irregular. For example, when using the 7×7 library with 250 markers, ArUco detects 112 false positives. Even though we would expect this number to increase with the library size, using the 7×7 library with 1000 markers results in 4 false positives. The average number of false positives detected by ArUco is 36 with the 7×7 libraries, and 1641 with all libraries.

6.2 Stability from Different Poses

To test the stability of marker localizations, we captured 1000 images of a 10 cm-wide stationary marker using a Logitech C920 webcam. For all frames, centers of detected markers are projected to the image using the respective estimated poses, and a mean center is found. Using the distances to the mean center, standard deviation is calculated as a metric of stability. See Figure 10 for the standard deviations of marker centers with different distances and viewing angles.

ArUco is not very stable, because it detects marker corners in a thresholded image. Nevertheless, four of such corners provide a marker center located with subpixel accuracy. RUNE-Tag is extremely stable, due to the large number of point correspondences used for pose estimation. However, it fails to detect more than 90% of the markers for viewing angles larger than 30° and distances farther than 100 cm. For this reason, we did not assess its performance beyond these

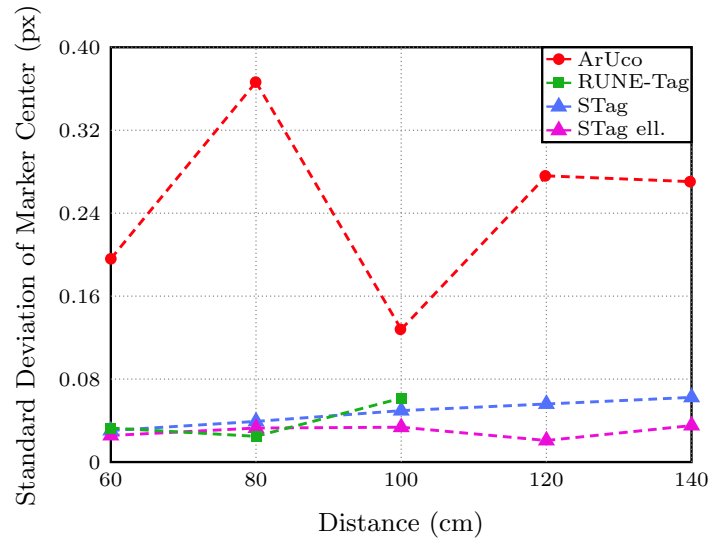
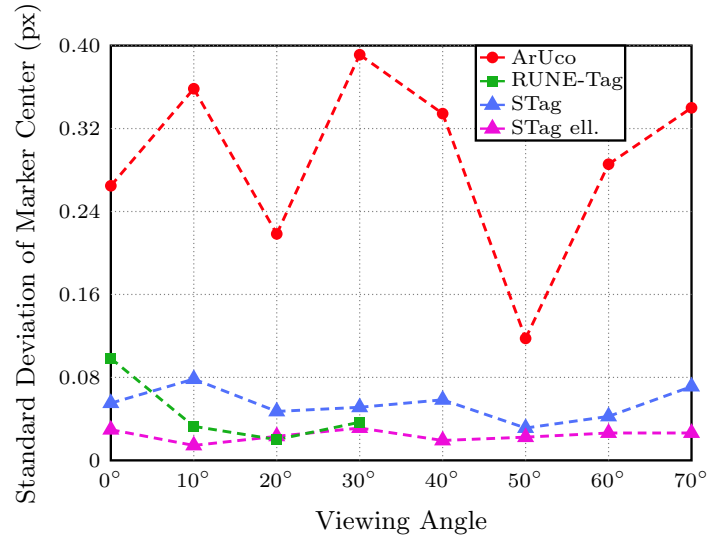


Figure 10: Standard deviations of marker centers with changing viewing angles and distances.

parameters. In contrast, both STag and ArUco were able to detect the markers in all images. STag provides stable localization across all viewing angles and distances in the experiment.

We have also presented the STag ellipse center stability in Figure 10. The ellipse center does not correspond to the marker center, thus using it as such will yield slightly inaccurate pose estimation. However, this discrepancy will be less significant where the marker size is relatively smaller than the viewing distance. In fact, RUNE-Tag uses the same assumption (that the ellipse center corresponds to the respective circle’s center in the real world) while solving PnP with no apparent penalty, because the ellipses are relatively small. Then, STag ellipse centers can be used as marker centers in tiled settings to sacrifice some accuracy for an even more stable pose estimation than the refined results.

7 Conclusion

The main contribution of the proposed marker system is improving pose stability with a refinement step. This is achieved by estimating the pose with the outer square border and refining it with the inner circular border. To our knowledge, this problem and the respective solution is unique in the literature in the way that a single conic correspondence is used, without additional projective constraints such as a point [14]. The proposed solution is significantly more stable than ArUco [13] with an 80% jitter variance reduction in average. Since it does not depend on a large number of fine details, it is significantly more robust across viewing conditions and runs an order of magnitude faster than RUNE-Tag [15].

For the multi-marker case, the inner circular borders can be used to estimate the pose with a multiple conic correspondence approach [37]. The alternative we have proposed is using the ellipse centers as stable, yet inaccurate correspondences of marker centers. This may cause some inaccuracy, but the stability of the point correspondences will yield an even more stable pose estimation.

The edge-segment based detection algorithm returns a small number of false marker candidates, and is feasible to be used for real-time applications. We demonstrated this with a novel approach, by trying to detect markers in an indoor scene recognition dataset. We believe that such extensive robustness experiments will be the norm in the following fiducial marker research.

We defined a lexicode generation algorithm for fiducial markers that is feasible to be used with longer codewords. Using this algorithm, we were able to generate marker libraries with various scales. This approach is more efficient than having marker variants with various bandwidths regarding error correction capability across the scale.

References

- [1] A. O. Balan, L. Sigal, M. J. Black, J. E. Davis, and H. W. Haussecker, “Detailed human shape and pose from images,” in *Proc. IEEE Conf. Comput. Vision and*

- Pattern Recognition*, pp. 1–8, 2007.
- [2] S. Sullivan and J. Ponce, “Automatic model construction, pose estimation, and object recognition from photographs using triangular splines,” in *Proc. IEEE Int. Conf. Comput. Vision*, pp. 510–516, 1998.
 - [3] M. Fiala, “Designing highly reliable fiducial markers,” *IEEE Trans. Pattern Anal. Mach. Intell.*, vol. 32, no. 7, pp. 1317–1324, 2010.
 - [4] J. Rekimoto, “Matrix: A realtime object identification and registration method for augmented reality,” in *Proc. Asia Pacific Conf. Comput. Human Interaction*, pp. 63–68, 1998.
 - [5] H. Kato, M. Billinghamurst, I. Poupyrev, K. Imamoto, and K. Tachibana, “Virtual object manipulation on a table-top AR environment,” in *Proc. Int. Symp. Augmented Reality*, pp. 111–119, 2000.
 - [6] X. Zhang, S. Fronz, and N. Navab, “Visual marker detection and decoding in AR systems: A comparative study,” in *Proc. IEEE/ACM Int. Symp. Mixed and Augmented Reality*, pp. 97–106, 2002.
 - [7] Make Magazine, “See the Secret Prototypes We Found in Valve’s VR Lab.” <http://makezine.com/2016/06/21/exclusive-see-the-secret-prototypes-we-found-in-valves-vr-lab/>, 2016.
 - [8] E. Olson, “AprilTag: A robust and flexible visual fiducial system,” in *Proc. IEEE Int. Conf. Robotics and Automation*, pp. 3400–3407, 2011.
 - [9] Amazon, “Amazon Prime Air’s First Customer Delivery.” <https://youtu.be/vNySOrI2Ny8?t=1m13s>, 2016.
 - [10] Boston Dynamics, “Atlas, The Next Generation.” <https://youtu.be/rV1hMGQgDkY?t=1m23s>, 2016.
 - [11] H. Kato and M. Billinghamurst, “Marker tracking and HMD calibration for a video-based augmented reality conferencing system,” in *Proc. IEEE/ACM Int. Workshop Augmented Reality*, pp. 85–94, 1999.
 - [12] M. Fiala, “ARTag, a fiducial marker system using digital techniques,” in *Proc. IEEE Conf. Comput. Vision and Pattern Recognition*, pp. 590–596, 2005.
 - [13] S. Garrido-Jurado, R. Muñoz-Salinas, F. J. Madrid-Cuevas, and M. J. Marín-Jiménez, “Automatic generation and detection of highly reliable fiducial markers under occlusion,” *Pattern Recognition*, vol. 47, no. 6, pp. 2280–2292, 2014.
 - [14] D. López de Ipiña, P. R. S. Mendonça, and A. Hopper, “TRIP: A low-cost vision-based location system for ubiquitous computing,” *Personal and Ubiquitous Computing*, vol. 6, no. 3, pp. 206–219, 2002.
 - [15] F. Bergamasco, A. Albarelli, L. Cosmo, E. Rodola, and A. Torsello, “An accurate and robust artificial marker based on cyclic codes,” *IEEE Trans. Pattern Anal. Mach. Intell.*, vol. 38, no. 12, pp. 2359–2373, 2016.
 - [16] L. Calvet, P. Gurdjos, C. Griwodz, and S. Gasparini, “Detection and accurate localization of circular fiducials under highly challenging conditions,” in *Proc. IEEE Conf. Comput. Vision and Pattern Recognition*, pp. 562–570, 2016.
 - [17] D. Wagner and D. Schmalstieg, “ARToolKitPlus for pose tracking on mobile devices,” in *Comput. Vision Winter Workshop*, 2007.

- [18] F. Bergamasco, A. Albarelli, E. Rodola, and A. Torsello, “RUNE-Tag: A high accuracy fiducial marker with strong occlusion resilience,” in *Proc. IEEE Conf. Comput. Vision and Pattern Recognition*, pp. 113–120, 2011.
- [19] S. Garrido-Jurado, R. Muñoz-Salinas, F. Madrid-Cuevas, and R. Medina-Carnicer, “Generation of fiducial marker dictionaries using mixed integer linear programming,” *Pattern Recognition*, vol. 51, pp. 481–491, 2016.
- [20] L. Naimark and E. Foxlin, “Circular data matrix fiducial system and robust image processing for a wearable vision-inertial self-tracker,” in *Proc. IEEE/ACM Int. Symp. Mixed and Augmented Reality*, 2002.
- [21] A. Xu and G. Dudek, “Fourier Tag: A smoothly degradable fiducial marker system with configurable payload capacity,” in *Proc. Canadian Conf. Comput. and Robot Vision*, pp. 40–47, 2011.
- [22] F. Bergamasco, A. Albarelli, and A. Torsello, “Pi-Tag: A fast image-space marker design based on projective invariants,” *Mach. Vision and Applicat.*, vol. 24, no. 6, pp. 1295–1310, 2013.
- [23] J. Sattar, E. Bourque, P. Giguere, and G. Dudek, “Fourier tags: Smoothly degradable fiducial markers for use in human-robot interaction,” in *Proc. Conf. Comput. and Robot Vision*, pp. 165–174, 2007.
- [24] R. Hartley and A. Zisserman, *Multiple View Geometry in Computer Vision*. Cambridge University Press, 2003.
- [25] D. Forsyth, J. L. Mundy, A. Zisserman, C. Coelho, A. Heller, and C. Rothwell, “Invariant descriptors for 3D object recognition and pose,” *IEEE Trans. Pattern Anal. Mach. Intell.*, vol. 13, no. 10, pp. 971–991, 1991.
- [26] C. B. Bose and I. Amir, “Design of fiducials for accurate registration using machine vision,” *IEEE Trans. Pattern Anal. Mach. Intell.*, vol. 12, no. 12, pp. 1196–1200, 1990.
- [27] S. Kirkpatrick, C. D. Gelatt, and M. P. Vecchi, “Optimization by simulated annealing,” *Science*, vol. 220, no. 4598, pp. 671–680, 1983.
- [28] J. Conway and N. Sloane, “Lexicographic codes: Error-correcting codes from game theory,” *IEEE Trans. on Inf. Theory*, vol. 32, no. 3, pp. 337–348, 1986.
- [29] J. H. Conway, “Sphere packings, lattices, codes, and greed,” in *Proc. Int. Congr. of Mathematicians*, 1994.
- [30] J. H. Conway and N. J. A. Sloane, *Sphere Packings, Lattices and Groups*. Springer New York, 1999.
- [31] M. Fiala, “Comparing ARTag and ARToolkit Plus fiducial marker systems,” in *Proc. IEEE Int. Workshop Haptic Audio Visual Environments and their Applicat.*, pp. 147–152, 2005.
- [32] C. Akınlı and C. Topal, “EDPF: A real-time parameter-free edge segment detector with a false detection control,” *Int. J. of Pattern Recognition and Artificial Intell.*, vol. 26, no. 1, p. 862872, 2012.
- [33] C. Akınlı and C. Topal, “EDLines: A real-time line segment detector with a false detection control,” *Pattern Recognition Letters*, vol. 32, no. 13, pp. 1633–1642, 2011.
- [34] A. Fitzgibbon, M. Pilu, and R. B. Fisher, “Direct least square fitting of ellipses,” *IEEE Trans. Pattern Anal. Mach. Intell.*, vol. 21, no. 5, pp. 476–480, 1999.

- [35] J. A. Nelder and R. Mead, "A simplex method for function minimization," *The Computer Journal*, vol. 7, no. 4, pp. 308–313, 1965.
- [36] A. Quattoni and A. Torralba, "Recognizing indoor scenes," in *Proc. IEEE Conf. Comput. Vision and Pattern Recognition*, pp. 413–420, 2009.
- [37] J. Kannala, M. Salo, and J. Heikkilä, "Algorithms for computing a planar homography from conics in correspondence," in *Proc. British Mach. Vision Conf.*, pp. 77–86, 2006.